QUARTERLY JOURNAL OF THE ROYAL METEOROLOGICAL SOCIETY
Q. J. R. Meteorol. Soc. **135**: 663–680 (2009)
Published online 30 March 2009 in Wiley InterScience
(www.interscience.wiley.com) DOI: 10.1002/qj.398

Wind profiler observations of a sting jet

G. A. Parton,[a†] G. Vaughan,[a]* E. G. Norton,[a] K. A. Browning[b] and P. A. Clark[c]
[a] *School of Earth, Atmospheric and Environmental Sciences, University of Manchester, UK*
[b] *School of Earth and Environment, University of Leeds, UK*
[c] *Joint Centre for Mesoscale Meteorology, University of Reading, UK*

ABSTRACT: Some of the most damaging surface winds experienced in midlatitude cyclonic storms have been attributed to a phenomenon known as a sting jet. Previous studies have deduced how sting jets develop from their midtropospheric origin, but there have been no direct observations of these wind features in the midtroposphere. During Windstorm Jeanette on 27 October 2002, the tip of the storm's cloud head passed over a VHF wind profiler at Aberystwyth, Wales, allowing the structure of a sting jet to be measured with high spatial and temporal resolution. These observations showed a multiple slantwise structure to the sting jet region, with two tails of increased winds that persisted after the passing of the cloud head aloft. Simulations by the Met Office Unified Model (UM) showed that the slantwise structure followed θ_w surfaces, and that the sting jet descended along θ surfaces as it passed over the UK, accelerating and drying during its descent. The horizontal and vertical scales of the observed structures are compatible with slantwise convection releasing conditional symmetric instability within the cloud head. Further observations of the sting jet were obtained by a UHF wind profiler at Cardington in Eastern England, where the sting jet had merged with the cold conveyor belt circulating around the storm. An unstable temperature profile in the lowest kilometre over Cardington enabled damaging gusts of strong winds to be brought to the surface in convective plumes; however, this strong vertical mixing was not represented correctly in the UM.

KEY WORDS VHF radar; slantwise convection; sting jet; mesoscale model; Windstorm Jeanette

Received 20 December 2007; Revised 29 December 2008; Accepted 29 January 2009

1. Introduction

In recent years new insights have been presented into the origin of the most damaging winds found in cyclonic storms that evolve according to the Shapiro–Keyser model of cyclogenesis (Shapiro and Keyser, 1990; Browning, 2004; Clark et al., 2005). These insights built on the observation by Grønås (1995) of damaging winds within the dry slot of such storms ahead of the characteristic cloud head as it hooks back around the warm seclusion. By a detailed analysis of surface winds and satellite imagery of the Great Storm of October 1987, combined with high-resolution mesoscale modelling, Browning and colleagues were able to attribute the most damaging winds to a coherent mesoscale wind feature they termed the *sting jet*.

According to this theory, the sting jet has its origin within the tip of the cloud head as it begins to encircle the central warm seclusion, late in the cyclone's development. Within this region multiple bands appear in satellite imagery with a scale consistent with conditional symmetric instability (CSI). Upward-moving moist branches of the circulation interleave with dry descending air, into which precipitation falls leading to evaporative cooling. Browning (2005) suggested that latent cooling by evaporation provided the descending air with greater impetus towards the surface, leading to damaging surface gusts.

Clark *et al.* (2005) used the mesoscale version of the Met Office Unified Model (UM) to simulate the sting jet in the October 1987 storm. They found that it was only when the number of vertical levels was increased from the standard 38 up to 90 that they were able to resolve a distinct jet-like feature, originating from within the cloud head, descending towards the tip and exiting in dry regions, before continuing its descent ahead of the cloud head. Using trajectory analysis, both forward from the cloud head and back from the area corresponding to the most damaging surface gust, they showed that the greatest descent occurred as a result of diabatic forcing, most likely attributable to evaporation in the cloud-head tip. The model exhibited a single coherent region of strong winds traceable from the cloud-head tip to the top of the boundary layer that existed over a number of hours, within which the descending air took around four hours to travel from around 650 to 900 mb.

In 1987, however, the only wind profile measurements were from radiosondes, which were not in the right locations to capture the sting jet. Thus, while the surface wind analysis, satellite imagery and model simulation all supported the sting jet concept, direct observational evidence of such a feature was lacking. It was therefore fortunate

*Correspondence to: G. Vaughan, School of Earth, Atmospheric and Environmental Sciences, University of Manchester, Simon Building, Oxford Road, Manchester, M13 9PL, UK.
E-mail: geraint.vaughan@manchester.ac.uk
†Now at Rutherford Appleton Laboratory.

that when a similarly evolving and damaging cyclone, later called Windstorm Jeanette, passed over the UK on 27 October 2002, its path took it over two wind profiling instruments that were well situated to capture a descending midtropospheric wind feature closely associated with the tip of the cloud head. The first of these was a VHF Doppler wind profiler, the Natural Environment Research Council (NERC) Mesosphere–Stratosphere–Troposphere (MST) radar located near Aberystwyth in Wales (52.42°N, 4.01°W). This showed the banded structure of the jet in the midtroposphere, and its persistence beyond the outer convex edge of the cloud head. The second radar was the University Facility for Atmospheric Measurement (UFAM) UHF boundary-layer wind profiler, deployed in Cardington, eastern England (52.06°N, 0.25°W) at the time of the storm. Two mesoscale runs of the UM provide further insight and link the observations of the two wind profilers: (a) the operational mesoscale UM at 12 km horizontal grid resolution, which provides synoptic and thermodynamic context but lacks the required resolution to resolve the sting jet; (b) a special run with a larger horizontal domain to capture the system's evolution and, crucially, an enhanced vertical resolution enabling the model to resolve the sting jet. However, the enhanced model run was not constrained by assimilation of synoptic observations and gradually departed from reality. Methods are described for overcoming this deficiency and allowing the model run to be compared with observations from the two radars.

2. Synoptic background

In the early hours of 27 October 2002 the UK experienced damaging surface winds associated with a cyclonic storm that became known as Windstorm 'Jeanette', resulting in widespread disruption to both power and transport. In addition, seven people were killed in the UK as a result of the high winds, and a further 23 across mainland Europe (http://www.torro.org.uk/TORRO/research/windstorms.php). Although Jeanette was not as severe as the Great Storm of October 1987, and indeed did not deepen explosively according to the standard definition of 24 mb in 24 hours (Sanders and Guyakum, 1980), there were many common features. The similarities between the two storms and the quality of the observations obtained during Jeanette therefore provide further insight into the nature of sting jets as a whole.

Figure 1 displays the depth of the central pressure of Windstorm Jeanette from its west Atlantic incipient stage at 1200 UTC on 24 October 2002 through to 1800 UTC on 27 October 2002. Its subsequent path took the storm over the southern UK to northern Europe, where it eventually decayed over Poland. The storm first deepened rapidly on 25 October, with a day of near-constant central pressure around 980 mb followed by a second deepening phase as it crossed the British Isles on 27 October. The sting jet observed here differs from the Great Storm of 1987 in being associated with this second deepening phase.

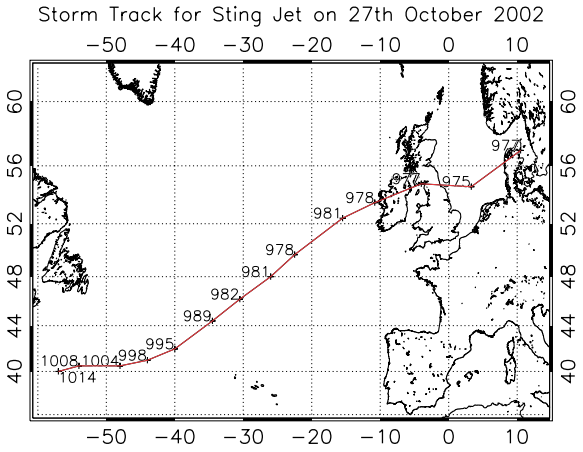

Figure 1. Mean-sea-level pressure (hPa) every 6 hours for Windstorm Jeanette from the UK Met Office's North Atlantic charts from 1200 UTC on 24 October 2002 to 1800 UTC on 27 October 2002. This figure is available in colour online at www.interscience.wiley.com/journal/qj

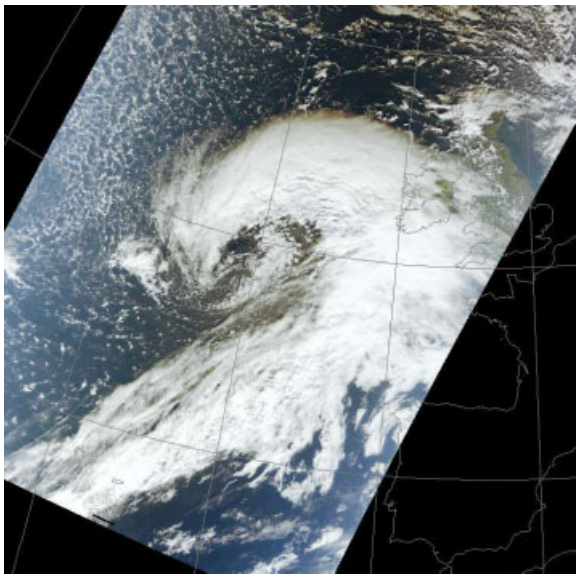

Figure 2. Composite image of channels 1, 4 and 3 (620–670 nm, 545–565 nm and 459–479 nm respectively) from the MODIS instrument aboard the Terra satellite for 1229 UTC, 26 October 2002. Image obtained from the University of Dundee Satellite Data Receiving Centre. This figure is available in colour online at www.interscience.wiley.com/journal/qj

Satellite imagery of the storm shows that the characteristic cloud head formed by 1200 UTC on the 26th, as shown in Figure 2. After this time the cloud head ceased its westward development (relative to the central depression) and began to hook back around the central low, as the system passed through to stage IV of cyclogenesis by 1200 UTC on the 27th (Figure 3). Evident behind and to the south of the cloud head at this time were shallow convective clouds, the motion of which (deduced from geostationary satellite images, not shown) followed the curvature of the outer cloud band, indicating low-level flow consistent with a cold conveyor belt (CCB; Browning, 1990).

Analysis of θ_w values on the 800 mb surface at 0000 UTC on 27 October from the operational UM

DOI: 10.1002/qj

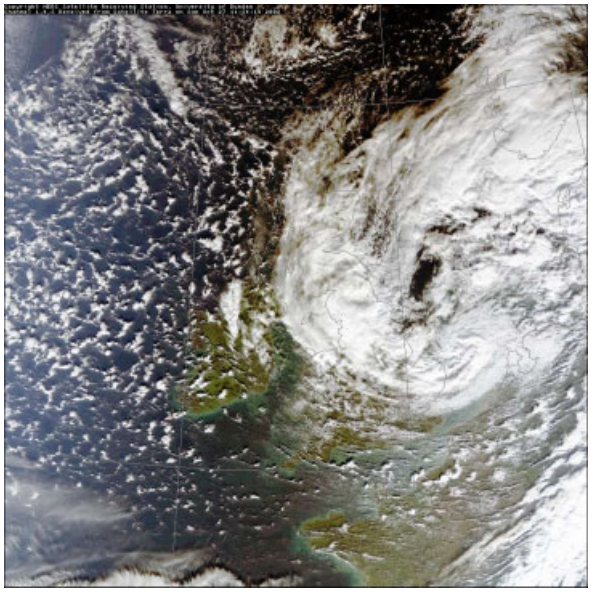

Figure 3. As Figure 2, for 1134 UTC, 27 October 2002. This figure is available in colour online at www.interscience.wiley.com/journal/qj

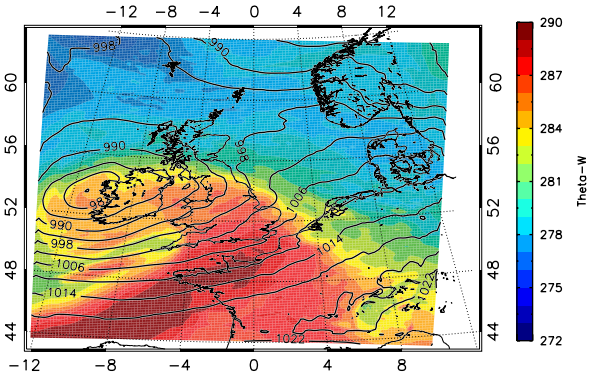

Figure 4. θ_w at 800 mb (shading) and MSL pressure (overlaid contours) from the UK Met Office's mesoscale Unified Model analysis at 0000 UTC on 27 October 2002. Notice the depression centre over western Ireland at this time. High θ_w values can be seen within the warm sector and through into the depression centre, while lower values are seen to the north, west and south of the depression centre. The strong gradients in θ_w indicate the location of the fronts. This figure is available in colour online at www.interscience.wiley.com/journal/qj

(Figure 4) shows that the cold front, marked as a strong gradient in θ_w, extended south-west from Cornwall and was well detached from the system's warm front. The strong θ_w gradient stretching from the Netherlands across the North Sea, through southern Scotland and onwards to the low pressure centre over western Ireland follows the line of a bent-back warm front. This front curved tightly southward on the western side of the depression centre. Between these two well-separated frontal surfaces a region of high θ_w air spread westwards towards the depression centre, while air with lower θ_w cut in from the west, following the cold front. After 0000 UTC the model showed colder air encircling the warm air within the depression centre (on the southern side of the bent-back warm front), forming a warm seclusion (and thus marking stage IV of the Shapiro–Keyser model of

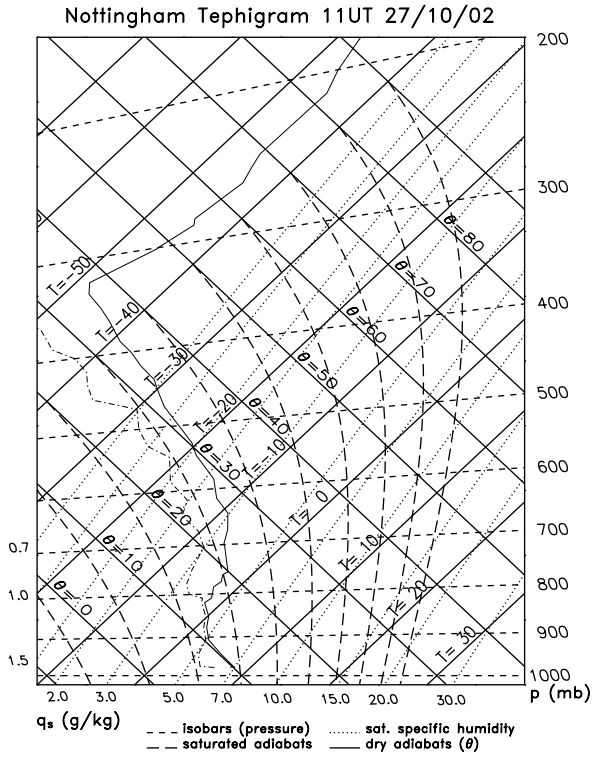

Figure 5. Radiosonde tephigram from Nottingham Weather Centre at 1100 UTC on 27 October 2002.

cyclogenesis) by 1200 UTC on the 27th (not shown). To the west of this warm seclusion a θ_w gradient of 5 °C over less than 100 km marked the transition to colder air. Upper air charts during this day showed a strong (typically 80–90 m s^{-1}) jet stream associated with the cold front.

Observational evidence from both Aberystwyth and Cardington supports the model analysis: wind profiler data from Aberystwyth presented in section 3 indicated a cold front clearly passing aloft, but losing its distinction below 4 km, and no clear evidence of a cold frontal passage from surface data at the site. Surface observations at Cardington did not record a change in air mass, but correlation with satellite imagery showed that the strongest surface winds (from 0600 to 1400 UTC on the 27th) occurred behind the cold front, but ahead of and during the passage of the cloud head aloft. In the middle of this passage, at 1100 UTC on the 27th, a radiosonde was launched from Nottingham Weather Centre (53.00°N, 1.15°W), 120 km north-north-west of Cardington. At this time, two rain bands lay approximately east–west beneath the cloud head (see later), and the radiosonde was released into the northernmost of the two. The radiosonde profile (Figures 5 and 6) shows two important features: firstly a low-level jet between 800 and 900 mb and secondly a layer with near-adiabatic lapse rate below 900 mb. From 900 to 800 mb the air is saturated, indicating the presence of a fast, moist, low-level air stream below the cloud head – i.e. the system's CCB.

DOI: 10.1002/qj

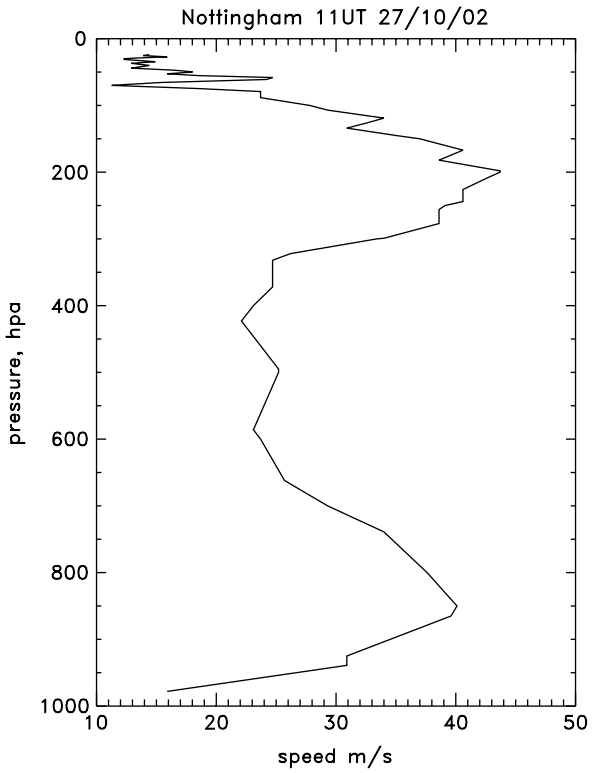

Figure 6. Wind speed profile from the Nottingham Weather Centre radiosonde at 1100 UTC on 27 October 2002.

3. Observations at Aberystwyth

3.1. MST radar observations

The MST radar at Aberystwyth provides continuous measurements of winds, echo power and turbulent intensity (spectral width) from 1.7 km to around 16–20 km altitude, depending on conditions. Key radar parameters are summarized in Table I; details may be found in Vaughan (2002).

Table I. Operational parameters for the MST and UHF wind profilers for 27 October 2002.

	MST radar	UHF radar
Location	52.42°N, 4.01°W	52.06°N, 0.25°W
Frequency (MHz)	46.5	1295
Time resolution (min)	2	2
Height resolution (m)	300	45
Height coverage	1.7–16 km	70–2500 m

MST radar data on 27 October 2002 were affected by interference. Despite applying windows in the spectral processing, its effect could not be completely eliminated, especially below 3 km from 0600–1030 UTC. The interference caused anomalously high spectral widths and so a conservative approach to data quality was adopted, removing all points where the spectral widths (after correcting for beam broadening) exceeded 1.2 m s^{-1}. This does result in some good data above 6 km being removed from Figures 7 and 8, but maintains data quality within the region of interest below 5 km. In addition, between 0630 and 0700 UTC the instrument experienced power interruptions, resulting in problems with transmission, and for this period data below 3 km have been discarded. These two procedures result in the white areas above 1.7 km in Figures 7 and 8.

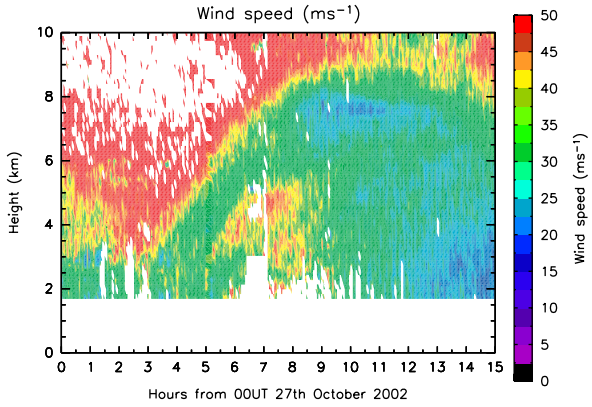

Figure 7. Wind speeds measured by the MST radar on 27 October 2002. Note the downward protrusion of strong winds just before the passage of the main cold front at ~0400 UTC at 4 km, followed by a secondary wind maximum from 0600–0900 UTC. Data are omitted where spectral width exceeded 1.2 m s^{-1} to remove any artefacts caused by the interference signal. This conservative approach removes good data from within the upper-level jet region, but this is not the focus of this study. This figure is available in colour online at www.interscience.wiley.com/journal/qj

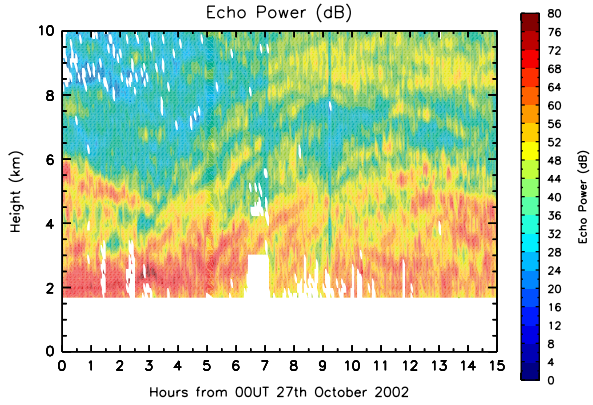

Figure 8. Echo power (dB) measured by the MST radar on 27 October 2002. White areas correspond to points blanked as described for Figure 7. This figure is available in colour online at www.interscience.wiley.com/journal/qj

The wind speeds measured by the MST radar (Figure 7) show a strong (>50 m s^{-1}) upper level jet at 10 km, agreeing well with the upper level charts for this day. This figure, together with the echo power (Figure 8), indicates that the system's cold front passed over the radar between 3 and 8 km from 0300–0800 UTC. (A cold front is delineated mainly by wind shear in MST radar profiles, but is often coincident with a maximum in echo power due to a gradient in absolute humidity and enhanced static stability (Reid and Vaughan, 2004).) As previously mentioned, the front, which led to a marked decrease in wind speed with time, is only evident above 3 km.

DOI: 10.1002/qj

About two hours after the passage of the cold front aloft, winds in the midtroposphere strengthened again. Between 0300 and 0900 UTC (Figure 7), wind speeds in excess of 37 m s^{-1} were measured below 5 km, at times increasing towards 50 m s^{-1}. Prominent slantwise banding is evident in the measured winds: the first band began around 3 km at 0500 UTC and extended upwards to 6 km by 0900 UTC, while a second band extended from 3 km at 0700 UTC up to 3.5 km at 0900 UTC, with a hint of a third band below that. A continuation of the first band may be discerned up to 1300 UTC, with a second 'wind tail' beneath, apparently emanating from around 2 km at 0800 UTC.

The echo power in Figure 8 indicates that the banded structures noted above have associated temperature and/or humidity structure in this region (section 7.2). This structure can more readily be seen in the composite plot of Figure 9, in which the primary bands of echo power (in red) and vertical wind shear (green) are superimposed on the wind contours. Clear in this Figure is the coincident echo power and shear band along the cold front, as discussed above. Below this, throughout the secondary wind maximum and continuing out into the wind tails, numerous parallel bands are seen in the echo power and wind shear. As will be shown later, these bands all slope along lines of θ_w according to the operational mesoscale UM. (Unfortunately, the radar was unable to resolve any vertical motions associated with these bands, as vertical winds were dominated by gravity (mountain) waves forced by the local topography.)

To summarize, the MST radar clearly observed a cold front passing over the site, traceable down to 3 km, below which its identity could not be distinguished. This was then followed by a low to midtropospheric wind maximum that developed two distinctive cores of stronger winds, the upper of which was stronger and began earlier. As the cloud head receded to the east, two distinct 'wind tails' were observed emanating from the wind maxima. Throughout this period there was parallel banding in the echo power and vertical wind shear.

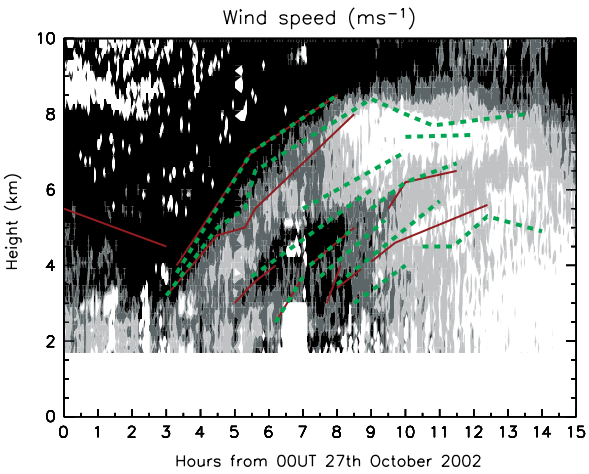

Figure 9. A composite plot showing key features from the MST radar data. Light grey, dark grey and black areas correspond to wind speeds greater than 29 m s^{-1}, 35 m s^{-1} and 40 m s^{-1} respectively. Solid (red) lines indicate prominent bands within the echo power greater than 48 dB, while the dashed (green) lines mark all areas of vertical wind shear $\geq$ 12 m s^{-1} km^{-1}. This figure is available in colour online at www.interscience.wiley.com/journal/qj

3.2. Relation of wind to cloud band

The key to understanding the midtropospheric wind maximum is its synoptic setting within the storm. Figure 10 shows infrared images from the Meteosat Satellite along with output from the UK Met Office's Nimrod rain radar network; the locations of the MST radar and Cardington sites are indicated by the black circles on each diagram.

At the onset of the midtropospheric wind maximum at around 0530 UTC, the cloud-head tip was still located to the west over Dublin (Figure 10(a)). At the same time the cloud associated with the cold front was located to the east and shallow cloud was seen in the dry slot between the cold front and bent-back warm front, a feature that remained throughout the passage of the storm. Beneath the cloud head was moderate to heavy precipitation, organized into a band that curved from its centre through to its tip (Figure 10(b)). By 0730 UTC the cloud-head tip arrived to the north of the MST radar site (Figure 10(c)). This was the time of the strongest winds above the MST radar in both the observed wind bands (at 4.5 and 3 km, Figure 7).

From 0930–1100 UTC the cloud head continued its eastward progression, moving further around the central depression. After 0930 UTC the radar lay south of the main cloud head; thus the wind tails extended beyond it, as did the banding in MST echo power. The satellite and rain radar images for these times (Figure 10(e)–(h)) show horizontal banding in precipitation at 0930 UTC over the Welsh hills, south of the main cloud head. It appears therefore that the generating mechanism for vertical and horizontal banding extended beyond the cloud head. One possible cause could be long-period gravity waves (Browning, 2005). However, when hodographs of the winds were examined throughout the period from 0700–1100 UTC there was no indication of the wind rotation characteristic of such waves. The most likely explanation is therefore some kind of slantwise instability, generating slantwise motions that eventually triggered the convective bands observed by the Nimrod radars. This is consistent with the CSI mechanism, although not definitive proof of its involvement; indeed it may point to dry symmetric instability (occurring in clear air) having a role as well. This point is further discussed in section 9.

3.3. Surface observations at Aberystwyth

Surface meteorological measurements were made at the radar site with a Campbell Scientific CR10 Climate Data Logger. Surface winds were measured with an A100R anemometer and a W200P wind vane from Vector Instruments, both located on a 10 m wind tower located at Frongoch Farm, 3 km west of the radar site, 140 m above mean sea level. Further details on the instruments,

DOI: 10.1002/qj

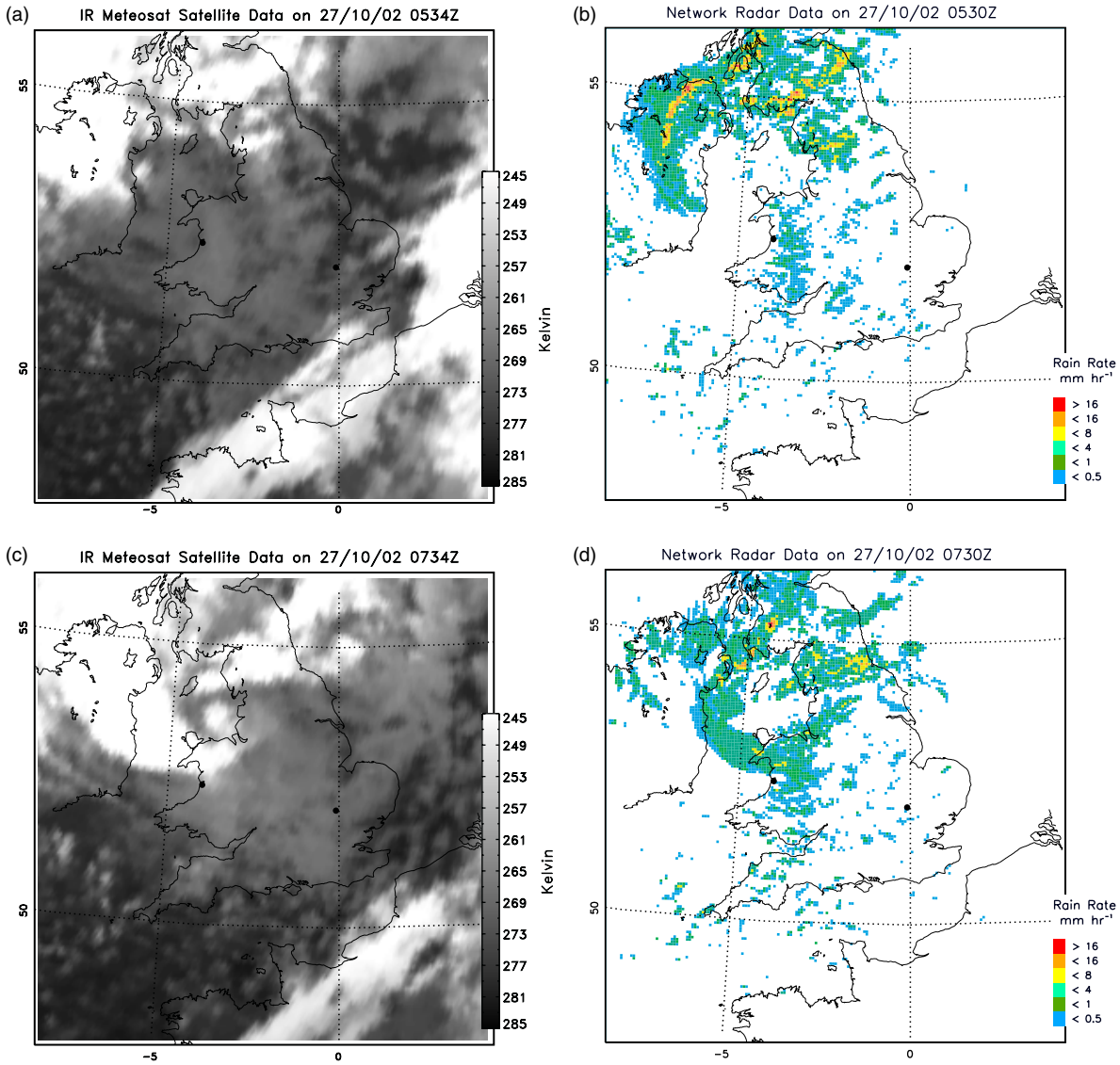

Figure 10. A sequence of images from the infrared (10.5–12.5 m) camera on the Meteosat satellite and corresponding rainfall rates according to the UK Met Office's Nimrod rain radar network for 0530 UTC ((a) and (b)), 0730 UTC ((c) and (d)), 0930 UTC ((e) and (f)) and 1100 UTC ((g) and (h)) on 27 October 2002. (Images courtesy of Dr. C.-G. Wang, University of Reading.) Black dots denote the locations of Aberystwyth (on the Welsh coast) and Cardington (near the meridian), where the two wind profilers were located. This figure is available in colour online at www.interscience.wiley.com/journal/qj

their accuracies and data acquisition can be found at http://mst.nerc.ac.uk.

As noted in section 2, it was difficult to identify a clear cold front passing over the site from the surface data (e.g. Figure 11). In contrast, the warm front arrived over the radar at around 2000 UTC on the 26th, marked by a sudden increase in surface wind speeds. At around 2300 UTC a decrease of 10% in RH (not shown) coincided with the arrival of the dry slot, but there was no change in wind speed at this time and the veering in direction ceased.

The vertical lines in Figure 11 correspond to the series of satellite and rain radar images (Figure 10). A small increase in wind speed (of the order of 3 m s^{-1}) occurred as the cloud-head tip arrived over the area (0730 UTC), but the surface wind speeds were around 20 m s^{-1} lower than the MST radar measurements above 2 km, and the maximum wind occurred 1–2 hours later. We show using the UM analyses that the increased low-level winds were due to the system's cold conveyor belt and not linked to the midtropospheric wind maxima at the MST radar site.

4. Observations at Cardington

4.1. UHF wind profiler measurements

The UHF wind profiler at Cardington was manufactured by Degreane Horizon, France, and is a mobile system operated by the Universities Facility for Atmospheric Measurements (UFAM). Its salient features are summarized in Table I. Like the MST radar, this wind profiler measures winds by the Doppler effect, with raw time resolution of 2 minutes. At these frequencies consensus averaging over 15–30 minutes is normally used to improve accuracy, but in the extreme conditions of this

DOI: 10.1002/qj

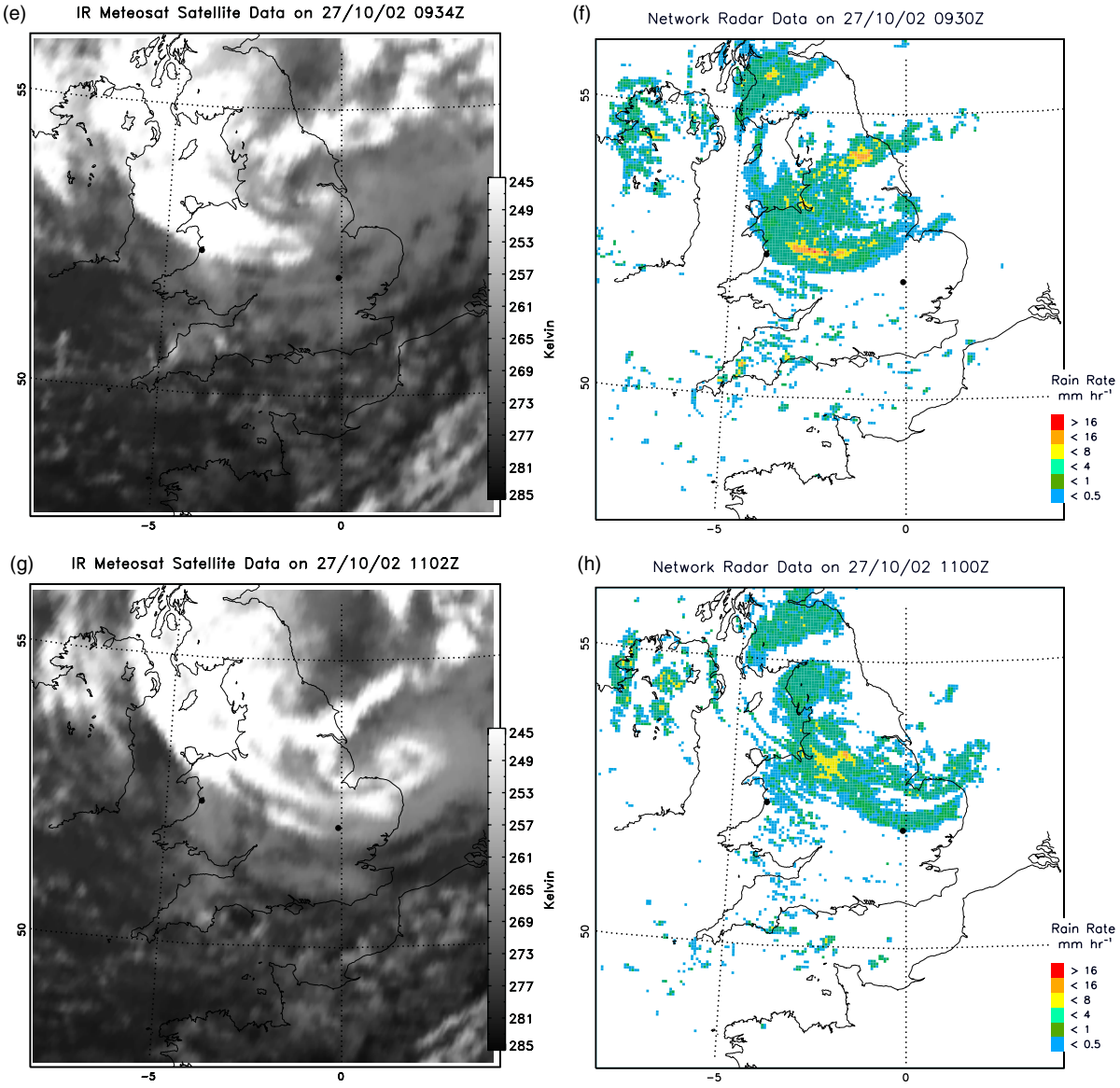

Figure 10. (*Continued*).

event the raw data were used unaveraged. Further details about the radar may be found in Norton *et al.* (2006).

From 0700–1300 UTC the UHF wind profiler showed a region of very strong winds (greater than 40 m s^{-1}) above 1000 m, while even at the lowest radar height gate (70 m) winds up to 35 m s^{-1} were measured (Figure 12). Below 1 km there were prominent 'plumes' of high wind speed extending towards the ground, correlating with high downward vertical winds measured by the radar (Figure 13), suggesting that precipitation may have been detected that affected the derivation of horizontal winds. Confirmation that showers passed over the radar came from the signal-to-noise ratio (not shown), which was greatly enhanced during episodes of high downward velocity, indicating the presence of particulate scattering.

However, even when removing those data with vertical velocities ≤ -1 m s^{-1}, prominent plumes of descending high-momentum air remained in the horizontal wind speed plots (Figure 14). The most notable of these were seen from 0900–1030 UTC and from 1200–1400 UTC. During this period of strong winds, the radar measurements show no vertical wind shear below 900 m. As shown below, this observation differs markedly from the mesoscale model simulation of this event.

4.2. Surface measurements at Cardington

Unfortunately, surface data for Cardington on this day were only available as 17 minute averages, meaning that the rapid fluctuations observed in the radar data (available every 2 minutes) could not be correlated with surface observations. However, by averaging the radar data over 17 minutes a comparison between winds at 400 m and 10 m becomes possible. They show (Figure 15) that the near-surface winds had a similar variation in strength during the day to those measured aloft. During the period of strongest winds (1000–1500 UTC) there was little difference in wind strength, while before and after this

DOI: 10.1002/qj

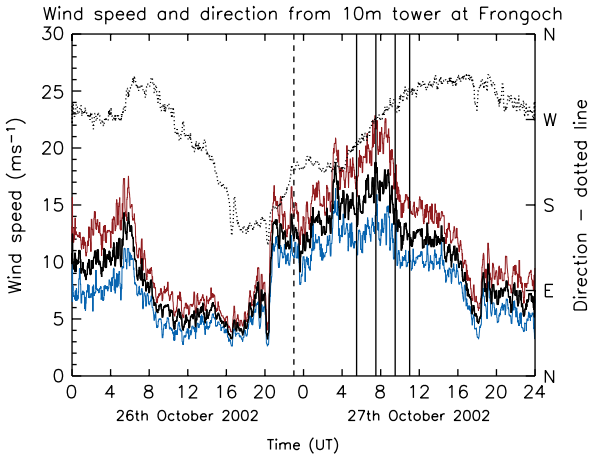

Figure 11. Ten-minute median (black), maximum (grey; red online) and minimum (grey; blue online) wind speeds and wind direction (dotted), measured on top of a 10 m mast at Frongoch, near Aberystwyth (140 m above mean sea level). The dashed vertical line indicates the expected time of the cold frontal passage derived by continuing the frontal line to the surface in the MST radar data. The four solid vertical lines correspond to the timings of the images in Figure 10. This figure is available in colour online at www.interscience.wiley.com/journal/qj

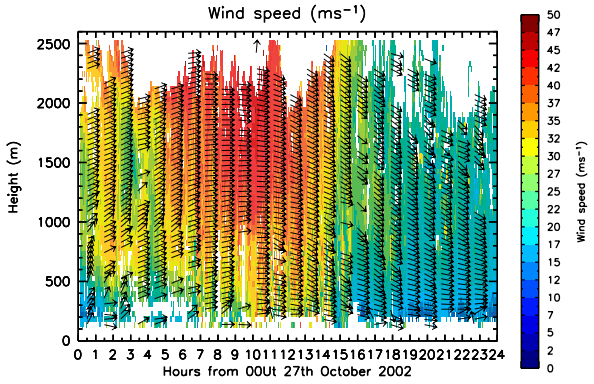

Figure 12. Wind speed and direction measured by the UHF wind profiler on 27 October 2002. This figure is available in colour online at www.interscience.wiley.com/journal/qj

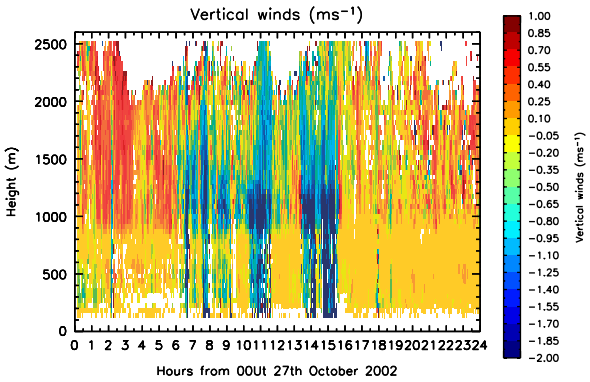

Figure 13. Vertical winds measured by the UHF wind profiler on 27 October 2002. This figure is available in colour online at www.interscience.wiley.com/journal/qj

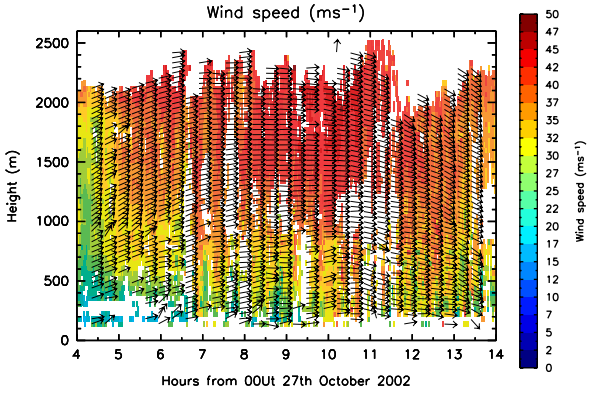

Figure 14. Wind speed at Cardington with areas corresponding to vertical winds ≤ -1 m s^{-1} blanked, removing returns from precipitation. This figure is available in colour online at www.interscience.wiley.com/journal/qj

period the 10 m winds were weaker. Likewise (not shown), the winds initially veered with height by up to 20°, but with the onset of the strongest winds this veer disappeared. As the system passed to the east of the site (from 1400 UTC onwards), and the winds abated, the wind veer re-appeared. This lack of any vertical shear during the strong wind period suggests a well-mixed lower layer of the atmosphere, consistent with the near-neutral stability shown by the Nottingham radiosonde.

Mean vertical winds were not measured at the surface, but standard deviations (s.d.) over 17 minute periods were available. These increased from 0.6 to 2.6 m s^{-1} during the strongest winds, indicating considerable gustiness at the surface (the s.d. subsequently reduced to 0.2 m s^{-1} as the winds abated). Such gusts are consistent with the downward-moving plumes seen in the profiler data.

The initial surface RH of 90–100% decreased to around 60% during the strongest winds and rose again to around 90% as wind speeds decreased. While this may indicate drier air moving in at low levels, the coincidence with downward-moving plumes is consistent with a drying of the low-level air by descent and mixing. Examination of the Nottingham radiosonde ascent (Figure 5) reveals that the saturated air from 900–800 mb, if brought adiabatically to the surface, would attain a RH of around 60–70%, similar to that observed.

In conclusion, strong winds extending from 200–2200 m were measured between 1000 UTC and 1400 UTC by the UHF wind profiler. At this time the 10 m tower winds were the same as those from the wind profiler at 400 m, showing the absence of any low-level wind shear. The descending plumes observed by the wind profiler, the increase in surface gustiness and the decrease in surface RH all attest to vigorous vertical mixing in the bottom kilometre of the atmosphere. Examination of the satellite images shows this to have been isolated convection rather than boundary-layer convergence lines as shown by Browning and Field (2004).

5. Representation of Windstorm Jeanette by the unified model

Having presented the observational evidence for the strong winds experienced during this storm, we now present simulations of the event using a mesoscale model.

DOI: 10.1002/qj

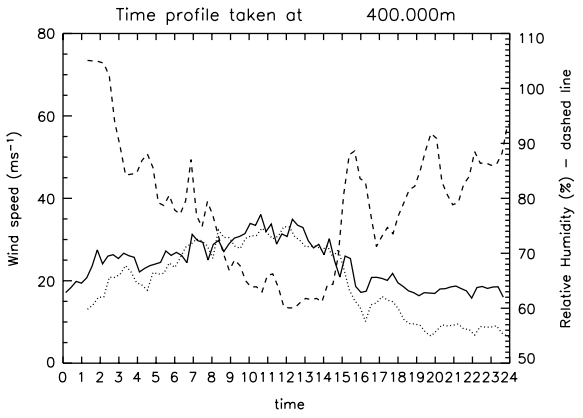

Figure 15. Time series of 17 minute time-averaged wind speed measured at 400 m by the UHF wind profiler (solid line) with 10 m surface wind speeds measured at Cardington (dotted line) on 27 October 2002. The dashed line gives relative humidity as measured at 1.2 m from the same site. Both the surface observations are 17 minute averages.

The motivation in this part of the article is (1) to relate the observations more firmly to theoretical concepts such as the cold conveyor belt and sting jet, (2) to determine whether the model is capable of reproducing the observations and (3) if so, to investigate what aspects of the model dynamics could be responsible. The remainder of the article is set out as follows: firstly we investigate mesoscale fields from the operational UM, then we show results from a run of this model with an enhanced domain and greater vertical resolution, and finally we develop diagnoses to apply to the latter to investigate the relation between the sting jet and CSI.

The two configurations of the mesoscale UM used in this study were as follows.

(1) The operational version of the model: analysis fields at 0000 UTC, 0600 UTC, 1200 UTC and 1800 UTC with +1 to +5 hourly forecasts from these analysis times. We refer to this as the *operational run*.
(2) As above but with 90, rather than 38, vertical levels (following Clark *et al.*, 2005) and an increased domain extended to the mid-Atlantic to capture the evolution of the system. We refer to this as the *enhanced run*.

The enhanced run was initiated from the $T + 3$ forecast of the global run of the UM run at 1200 UTC on 26 October. The model evolved freely from this initial time to produce forecasts for +1 to +32 hours. To allow for spin-up only the period after 1900 UTC on 26 October is used in this study. The set-ups of the models are summarized in Table II.

6. Operational UM simulation

As the operational mesoscale model includes data assimilation, the development of the model storm corresponds well to that observed, both in timing and position. The simulation allows us therefore to position the wind profiler observations correctly within the synoptic context, and to identify the canonical features described in Table III.

The UM θ_w field presented in Figure 4 delineates the positions of the fronts and warm seclusion at 0000 UTC on 27 October. In addition, the model indicated (not shown) that the seclusion's northern boundary was defined by a band of dry potential vorticity with 1–3 PV units at 850 mb, a feature repeated on other pressure surfaces up to 600 mb where it began to lose its identity. To the south of the seclusion a well-defined tongue of dry air could be traced from the upper troposphere with high PV values indicative of a tropopause fold (not shown). This formed part of the dry intrusion that descended from the upper and midtroposphere. The UM wind fields for this period also showed a CCB wrapping around the system underneath the upper cloud deck, with typical speeds ranging from 30–45 m s^{-1} as it entered the southern quadrant of the storm. Typical properties of the CCB and tropopause fold/dry intrusion for this study are summarized in Table III. It should be noted that the dry PV, used here to identify the dry intrusion, can in general take high values in a CCB due to moist diabatic processes, but this was not the case here.

6.1. Comparison of operational UM fields with MST radar wind profiler measurements

To compare the model with the MST radar wind and power profiles, a vertical sounding was taken at each hour from model data interpolated to 52.42°N, 4.01°W. The results are shown as contours over the MST radar measurements in Figure 16. The model correctly depicted the upper level jet in the early hours of 27 October, with strong shear coincident with that in the MST radar data marking the cold front. The model also placed a secondary wind maximum where the upper band of strong winds was measured by the radar (at 4 km and around 0700 UTC), although its speed was about 10 m s^{-1} weaker than observed. There is also some indication of the tail of this wind feature as it extended to 6 km by 1000 UTC. The model failed, however, to reproduce the lower wind band at 3–3.5 km. Finally, a low-level wind maximum with a core wind speed of 36 m s^{-1} was depicted around 0800 UTC at 1 km, the typical height of the system's CCB.

To further characterize these features, a synthesis of model variables is presented in Figure 17. From this, along with the properties of the CCB, sting jet and dry intrusion summarized in Table III, we see that the lowest wind feature is indeed the CCB, with a θ_w of 281 K at its core, a RH > 80% and dry PV < 1 PV unit. The upper level jet (centred at 9 km at 0300 UTC) is characterized by θ_w > 285 K, < 40% RH and dry PV > 1 PV unit, corresponding to the dry intrusion. These features are distinct from one another and from the mid-level wind maximum, labelled SJ, centred at 4.5 km at 0700 UTC. This secondary wind maximum is located at the leading edge of the high RH values corresponding to the cloud head, in a region between the high PV values of the dry

DOI: 10.1002/qj

Table II. Model parameters used in this study.

UM mesoscale model type	Operational	Enhanced
UM model version	5.3	5.3
Horizontal resolution	0.11° x 0.11°	0.11° x 0.11°
Analysis times (forecast periods)	0000, 0600, 1200, 1800 UTC (+1 to +5 hour forecasts)	1500 UTC 26/10/02 (+1 to +32 hour forecasts)
Model vertical resolution (ie number of model levels)	38	90
Pressure levels used	1000 mb to 50 mb in 50 mb steps	1000 mb to 25 mb in 25 mb steps

Table III. Typical parameters of the system's CCB, dry intrusion and sting jet from the operational mesoscale UM. The dry intrusion is the extensive tongue of dry air descending from the upper troposphere ahead of the cloud head and behind the cold front.

Parameter	CCB	Dry intrusion	Sting jet
Relative humidity with respect to ice (%)	≥90	≤40	≥80
θ_w (K)	281	285–288	283
Dry PV (10^{-6} K kg^{-1} m^2 s^{-1})	<1	>1.5	≤1
Typical altitude (km)	0.5–1.5	2–8	4–5

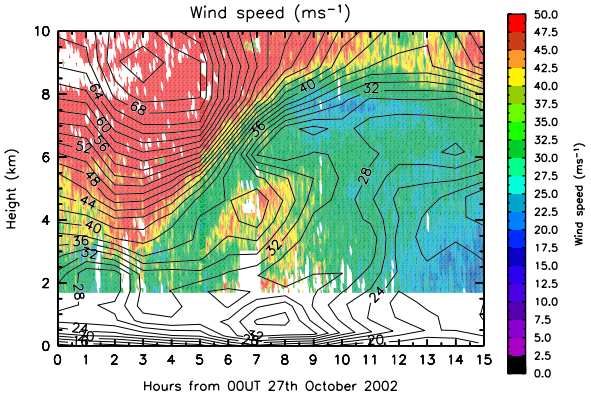

Figure 16. MST radar wind speeds (colour) with corresponding values from the operational UM fields overlaid as contours. Note that below the main jet stream the operational UM depicted two separate features between 0700 UTC and 0900 UTC: a wind maximum at 4–5 km and the CCB below 2 km. Unreliable MST radar winds have been blanked as described in the text. This figure is available in colour online at www.interscience.wiley.com/journal/qj

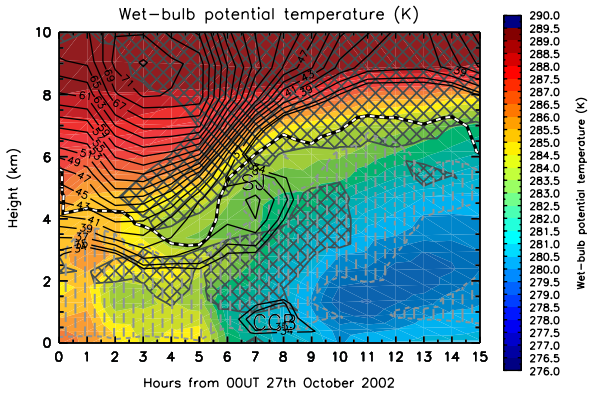

Figure 17. A synthesis of data from the operational UM above the MST radar site. Here θ_w (coloured background) shows the differing natures of the wind features indicated by the SJ and CCB labels. Winds are contoured in bold black lines at 34 and 35 m s^{-1} then every 2 m s^{-1} above this, while relative humidities ≥ 80% are denoted by the vertically lined area and the 50% relative humidity contour is marked by the thick white and black line. Dry potential vorticity ≥ 1 PV unit is marked by hashed regions. This figure is available in colour online at www.interscience.wiley.com/journal/qj

intrusion and the cloud head. The location of this jet at the tip of the cloud head, distinct from both the CCB and dry intrusion, is characteristic of a sting jet.

The echo power from the MST radar is compared with the model θ_w in Figure 18. The banding in echo power clearly follows the slope of the θ_w field, confirming that these banded features lie along θ_w surfaces. We argue later that this supports the contention that CSI caused the banding seen within the cloud head, and contributed to the generation of the sting jet.

6.2. Limitations of the operational UM

On the face of it the operational model simulated the observations very well. However, data from the MST radar are assimilated into the UM during each analysis period; it is unsurprising therefore that the overall structure of the measured wind field was reproduced. To examine the effect of assimilating the MST radar wind profiles, and hence the ability of the model to resolve the mechanisms that generate sting jets, the +1 to +12 hourly forecast fields from the 0000 UTC analysis were used to create a corresponding figure to Figure 17. This figure, not shown here, did not show a clear sting jet, although both the main jet and CCB were clearly represented. This suggests that the sting jet in Figure 17 resulted from the assimilation scheme, not the model dynamics, and so the model fields cannot be used to examine its development. However, the temperature and humidity structure remained broadly the same, allowing us to conclude that the banding seen in the radar echo power followed θ_w surfaces and that such banding existed within the cloud head.

The limited value of operational mesoscale model data for investigating this event is further supported

DOI: 10.1002/qj

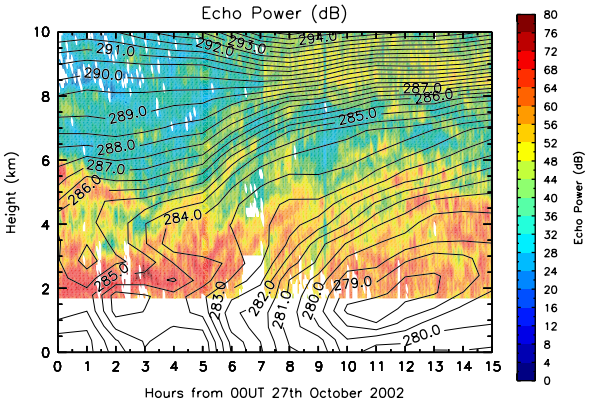

Figure 18. MST radar echo power with θ_w values from operational UM data overlaid. This figure is available in colour online at www.interscience.wiley.com/journal/qj

by section 7 of Schultz and Schumacher (1999), who reviewed mesoscale model studies of moist symmetric instability (hereafter MSI), of which CSI is a subset. Citing works by Persson and Warner (1993) and Ducrocq (1993), Schultz and Schumacher gave the minimum horizontal and vertical resolution required to capture the most unstable modes of unforced, hydrostatic, nonlinear MSI as 15 and 0.17 km respectively. Given that such instabilities are similar to CSI and are released in slantwise circulations, such resolution requirements apply here too, and show that the vertical resolution of the operational model (roughly 0.5 km at 4 km) is insufficient to resolve these features.

7. Enhanced mesoscale model run and comparison with MST radar

We now investigate whether doubling the vertical resolution of the UM simulation enables it to reproduce a sting jet, following the successful experiment of Clark *et al.* (2005) for the Great Storm of 1987. As the model in this case was unconstrained by an assimilation scheme, it gradually diverged from reality over the course of 36 hours, depicting a more intense system than that observed, with a more prominent warm seclusion and stronger gradients in θ_w across the frontal surfaces. The values of θ_w associated with the warm sector and warm seclusion were 2–3 K higher than in the operational model. Wind speeds tended to be stronger, and wind maxima and minima were narrower than in the lower resolution model. Other than this, the salient features of the simulation were similar to those in Table III.

As it passed over the UK, the storm in the enhanced UM simulation spiraled further around its centre than its counterpart in the operational model. Thus, times in the following discussion will be different for the model and the observations, and model times should be read as labels corresponding to stages in the system's evolution, and not confused with the corresponding times for the real storm. For example, since the whole system evolved faster than in the operational model, the period of interest in this enhanced run was from 0300 model time, as opposed to 0700 UTC onwards in the operational analysis and reality.

This departure from reality meant that the MST radar measurements could not be directly compared with the model fields at the radar location. Rather, a search was made for for pseudo-locations that bore the same relationship to the storm morphology and evolution as the MST radar did to the real one. The first stage in identifying these pseudo-locations was to note the development of the θ_w, dry PV and wind fields, and compare these with corresponding fields from the operational UM and with observations. Secondly, comparisons were made between the cloud-head tip as seen in Meteosat imagery (e.g. Figure 10) and the position and shape of the cloud head within the enhanced model, using the approach of Clark *et al.* (2005). However, comparisons of actual and synthesized satellite images did not lead to useful pseudo-locations, because of the different evolution of the storm in the two cases. Thus, algorithms were developed to search within the model fields for the distinctive features in the MST radar data highlighted earlier. Before these algorithms are introduced we first show that the model did indeed reproduce features similar to the radar measurements.

7.1. Zonal cross-sections

Zonal and meridional cross-sections were taken near the cloud-head tip when the cloud head lay to the south of the central low (from 0400 to 1000 model time). Examination of the relative humidity allowed regions of ascent and descent to be identified, e.g. a wind feature residing in drier air than its surroundings was likely to have undergone descent. This allowed the sting jet and CCB to be distinguished. One such plot, taken along 50.76°N, can be seen in Figure 19, which clearly identifies the dry intrusion by its very low relative humidity ($< 10\%$). In addition, a low-level wind feature can be seen around 2 km in a dry region ($< 50\%$) between 1–4°W, extending into a region of higher RH values associated with the cloud head. Further west, from 8–12°W, the wind field between 3 and 6 km resembles the double wind bands seen in the MST radar data. Through the centre of these bands there is a band of high relative humidity which continues beyond them to 20°W.

Comparing this with Figure 16 of Clark *et al.* (2005), the resemblance is encouraging. In both cases a core of strong winds can be traced back from a low-level dry region into the cloud head. Further west the wind contouring in both cases indicates features similar to the double peak in the MST radar data.

7.2. Model-derived simulations of MST power plots

According to the theory of clear air wind profilers (Ottersten, 1969; Gage *et al.*, 1981) the returned signal depends on changes in the gradients of refractive index in the air within the sounding column. These depend in turn on changes both in the specific humidity and potential

DOI: 10.1002/qj

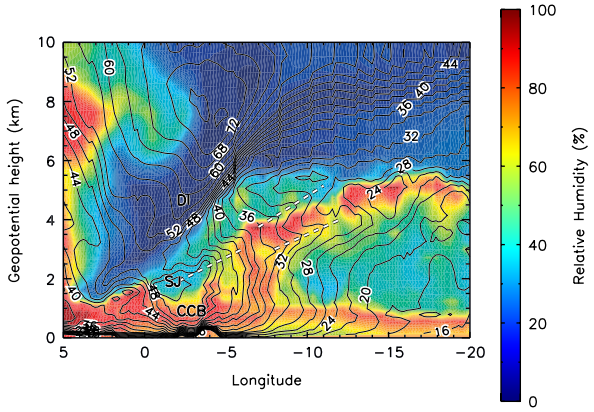

Figure 19. Zonal cross-section along 50.76°N from the enhanced model run at 05 h model time on 27 October. Coloured contours show relative humidity with respect to ice while overlaid contours are isotachs at 2 m s^{-1} intervals. Note that the x axis runs east–west in this plot to facilitate comparison with Figures 7 and 8. White dashed lines denote the sting jet and double wind maxima, with the dry intrusion, sting jet and cold conveyor belt depicted by DI, SJ and CCB respectively. This figure is available in colour online at www.interscience.wiley.com/journal/qj

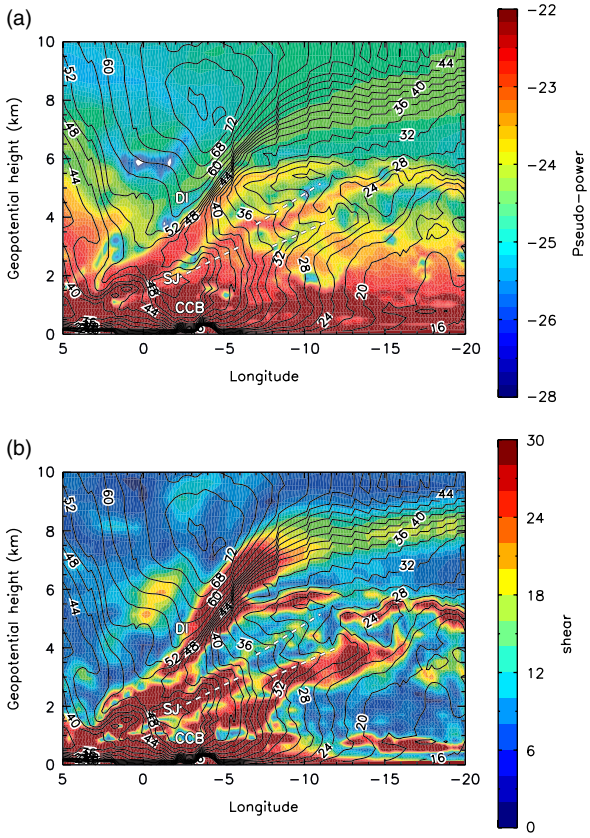

Figure 20. Zonal cross-section along 50.76°N from the enhanced model run taken at 05 h model time on 27 October 2002. (a) Model-derived echo power parameter P_{mod} (coloured contours) with isotachs at 2 m s^{-1} intervals overlaid. (b) Vertical wind shear with isotachs at 2 m s^{-1} intervals overlaid. Annotations are as Figure 19. Note that the x-axis runs east–west in these plots to facilitate comparison with Figures 7 and 8. This figure is available in colour online at www.interscience.wiley.com/journal/qj

temperature. Accordingly, model vertical profiles were used to derive a simulated radar power P_{mod}, defined as

$$P_{\mathrm{mod}} = A \log_{10}\left(\frac{M^2}{z^2}\right), \qquad (1)$$

where M is the vertical gradient of potential refractive index, z is the geopotential height and A an arbitrary constant. M is defined as follows (Ottersten, 1969):

$$M = C\frac{p}{T}\left(\frac{\partial \ln\theta}{\partial z} + \frac{15\,500q}{T}\frac{\partial \ln\theta}{\partial z} - \frac{7750}{T}\frac{\partial q}{\partial z}\right), \qquad (2)$$

where p, T, q, θ and z are pressure, temperature, specific humidity, potential temperature and height respectively, and $C = -77.6 \times 10^{-6}$.

A zonal cross-section of P_{mod} along 50.76°N at 0500 h model time is shown in Figure 20. Assuming a steady eastward motion for the storm, and a slower time-scale for its evolution than for its translation, this should be comparable to the radar time–height plots.

Similar relationships to those in the MST radar data are seen between the model-derived power and wind fields when Figure 20(a) is compared with Figures 8 and 9: high values of P_{mod} at low levels with bands of high power extending upwards and westwards. A maximum in echo power between the two wind maxima in the region 8–10°W, 3–5 km corresponds very well with a similar feature in Figure 9, and leads down to the core of strong winds at 2°W, 1.8 km. Likewise, when horizontal wind shear (Figure 20(b)) is compared with Figures 8, 9 and 20(a), the shear layers are found to lie parallel to the echo bands, as seen in the MST radar data.

We therefore conclude from examining both the wind and thermodynamic fields that the enhanced model produced structures very similar to those observed by the MST radar (although not at the same time and place as the observations because the model was unconstrained by observations). To relate the measurements made by the two wind profilers, and show that the sting jet observed over Aberystwyth was later observed at a much lower altitude over Cardington, we first need a method of identifying distinctive features in the model fields.

7.3. Identifying wind features in the model fields

Two algorithms were applied to the model fields at 0600 h model time to locate the double wind maximum and the descending sting jet. These were developed by trial and error using a number of possible criteria to separate the features of interest from the surrounding flow; thus they are somewhat arbitrary and should not be assumed to apply in all cases of this type. They are best understood by reference to Figure 19, where the double wind feature straddles the band of high RH around 4 km between 8 and 12°W, and the descending sting jet appears in the dry air around 2 km, 1–4°W. The double wind algorithm consisted of three stages:

(1) seek a relative humidity maximum between 3 and 5.5 km where moist PV $\leq$ 1 PV unit, wind speeds $>$ 22 m s^{-1} and RH $>$ 40%;

DOI: 10.1002/qj

(2) locate local wind maxima above and below the RH maximum, in the altitude range 2.5 km to 5.7 km;
(3) if these wind maxima have RH lower than the RH maximum and vertical separation of at least 750 m, a double wind feature is identified.

Moist PV is used here rather than dry PV because we are seeking to identify a feature in a moist environment, where the dry PV could be changing.

To identify the descending sting jet, the low relative humidity values associated with the feature had to be distinguished from those of the dry intrusion. To achieve this the algorithm was restricted to moist isentropes intersecting the cloud head, i.e. θ_w = 281.5–285.5 K, with moist potential vorticity < 0.5 PV units and relative humidity between 40 and 80%. A sting jet was identified if the wind speed in such a region exceeded 25 m s^{-1} between 2 and 4 km, provided the local wind maximum coincided with a local relative humidity minimum; the algorithm was therefore designed to search ahead of the cloud head.

Figure 21 shows the horizontal extent of features identified by the two algorithms at 0600 h model time, in relation to the outgoing broad-band radiance temperature. Areas where the descending sting jet was detected are shown in red while the areas returned by the double-wind maximum algorithm are shown in white. The sting jet is ahead of the cloud head, and the double wind maxima near its outer convex edge, consistent with the MST radar observations.

7.4. Origin and development of the features

Having identified similar features to those seen by the MST radar within the enhanced model fields at one model time (0600 h), we now examine the origin and development of these features using trajectories. The aim here is to determine the relation of the features to the cloud head (going back in time) and to low-level wind maxima (going forward in time). Trajectories were initiated at 0600 h model time on the 27th at a fifth of all grid points within the red and white areas shown in Figure 21, and taken back to 1900 h model time on the 26th and forward to 1000 h on the 27th. Trilinear interpolation was used between grid points and linear interpolation between model time steps (available at each hour) to calculate the trajectory vector at each step. As a quality check, any trajectories that exhibited a change in θ_w of more than 0.2 K per hour were not used for further analysis; this affected mostly trajectories below 3 km.

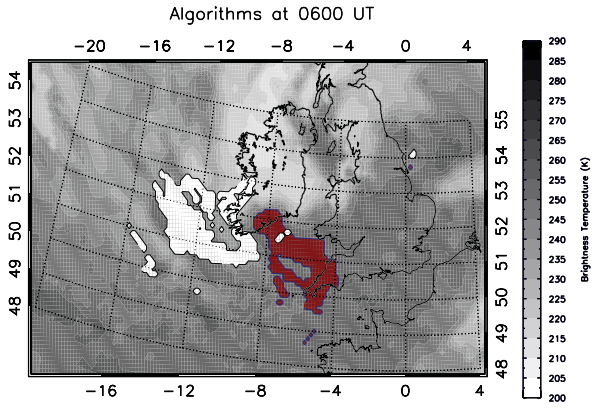

Figure 21. Simulated outgoing infrared radiation, with locations identified by feature-finding algorithms overlaid for 0600 h model time. Areas where a descending sting jet was found are shown in red; areas corresponding to a double-tailed wind feature are shown in white. This figure is available in colour online at www.interscience.wiley.com/journal/qj

Examples of trajectories within the sting jet region are presented in Figure 22, illustrating their general descent and drying after around 0200 h model time; the overall descent was about 1 km over 10 hours. During this period wind speeds along the trajectories increased from 15–25 m s^{-1} to around 50 m s^{-1} by 0800 h. After this there was a slight decrease at the lower levels (probably due to boundary layer processes within the model) while the upper levels increased by a further 5 m s^{-1} over the next 2 hours. Potential temperatures cooled by 1–2 K at the upper levels during the descent, while the lower levels remained fairly isentropic. The trajectories remained to the south of the cloud-head tip as it moved around the central depression. Prior to 2300 h, they tracked close to the cloud head; after this they moved eastward away from its tip, confirming that the air descended ahead of the cloud head. According to the model, therefore, the sting jet descended almost isentropically by about 1 km in 12 hours, accelerating considerably as it did so.

Corresponding trajectories for the double wind maximum (not shown) showed broadly similar behaviour to Figure 22, with overall descent by about 1 km and drying to around 30–50% RH. On overlaying the trajectories during the period of descent on the outgoing infrared for 0200 UTC (Figure 23), the area of the double wind maximum is seen to originate from the rear of the main cloud head and the secondary cloud feature to the south-west of the main cloud head. Subsequently, the trajectories moved eastward, remaining to the rear of the cloud head as it began to hook around the southern quadrant of the storm. Unlike the sting jet trajectories, there was no displacement relative to the tip of the cloud head during the period of descent.

8. Enhanced mesoscale model run and comparison with UHF profiler

We now turn to the low-level wind observations at Cardington, and the representation of these in the enhanced model. The passage of the system's cold conveyor belt over Cardington was inferred from Figures 3 and 6, but the strong winds before the arrival of the cloud head over Cardington require closer examination. We now present selected fields from the enhanced UM to suggest that this period corresponded to the descending sting jet. The interpretation here is more complex than for the MST radar because the model suggests that the descending sting jet and the CCB merged into one region of strong winds, the components of which could

DOI: 10.1002/qj

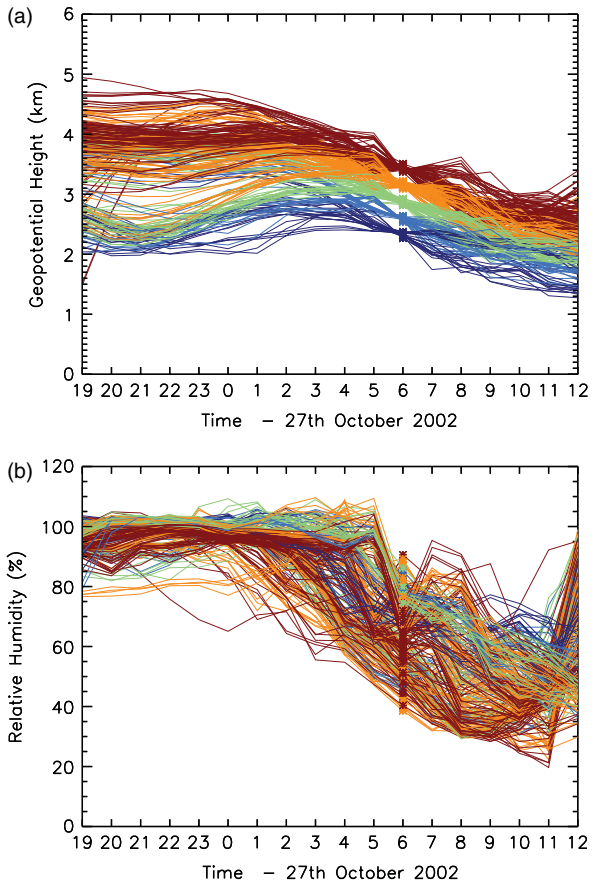

Figure 22. (a) Geopotential heights and (b) relative humidities along trajectories initiated in groups at 50 mb intervals from 850–650 mb above the area returned by the sting-jet-finding algorithm. These are taken back to 1900 h model time on 26th October and forward to 1200 h to show subsequent evolution. Different colours denote different initial pressure. This figure is available in colour online at www.interscience.wiley.com/journal/qj

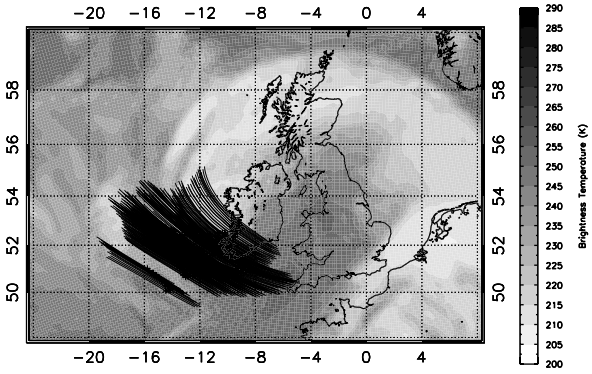

Figure 23. Simulated outgoing infrared radiation at 0200 UTC, 26th October 2002 from the enhanced model with trajectory tracks initiated at 750 mb at 0600 UTC from within the area identified with a double wind feature. These trajectories have been taken back to 0200 UTC and forward to 0800 UTC.

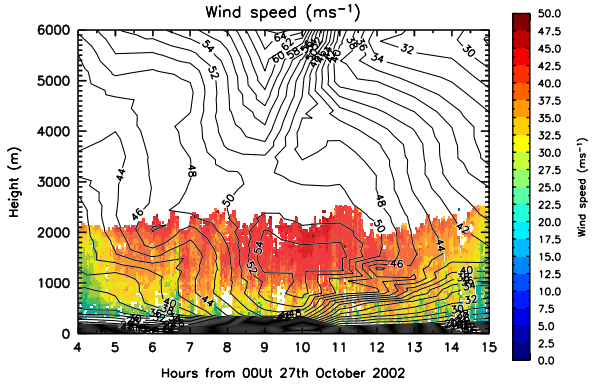

Figure 24. Wind speeds from the UHF profiler (colours) with winds from the enhanced UM run overlaid as contours every 2 m s^{-1}. A time shift of +2 hours has been applied to the model fields for this plot. This figure is available in colour online at www.interscience.wiley.com/journal/qj

not be distinguished from the wind profiler observations alone.

As noted above, the enhanced model run produced a storm that was more intense, passed through cyclogenesis quicker and was located farther south than the actual storm. To compensate for this the following discussion focuses on an equivalent part of the storm to that passing over Cardington. Unlike the MST radar site, it was possible to find fixed geographical locations in the enhanced UM simulation that experienced a similar meteorological evolution to that observed at Cardington. One of these, at 51.29°N, 0.08°W, was chosen as the Cardington pseudo-location. The system evolved more quickly in the model simulation than in reality, and in the following comparison with observations a time shift of 2 hours has been applied to model fields.

8.1. Comparison of UHF radar with model

A time series of winds at this location, overlaying the measured and time-shifted model winds, is presented in Figure 24. Distinct from the upper level jet, a low-level wind maximum is shown below 2 km in the model field, corresponding to that observed between 0900 UTC and 1100 UTC by the wind profiler. The strongest model winds were 5 m s^{-1} greater than measured and abated less suddenly than the measurements. They also show a tongue of strong winds at 1000 h in the (time-shifted) model extending down from 1000 m to 500 m, suggesting either a lower wind feature or a mechanism that is present to bring higher momentum air down from above. We now examine other model variables to investigate the nature and origin of the low-level wind features.

In Figure 25 a synthesis of various parameters from the high-resolution model is presented, in an analogous way to Figure 17. The high θ_w, low relative humidity and elevated PV values at the top left of the diagram are typical of the dry intrusion. Below this is the low-level wind maximum that would at first appear to be the CCB, by examination of θ_w, but its core is both dry (<50% relative humidity) and above a region of high potential vorticity. There is a moist layer below this PV anomaly, in which wind speeds remain high, with the tongue of high winds at 0800 UTC where θ_w is slightly lower. This region is more consistent with the CCB. We propose that the low-level wind maximum is in fact a merger of two

DOI: 10.1002/qj

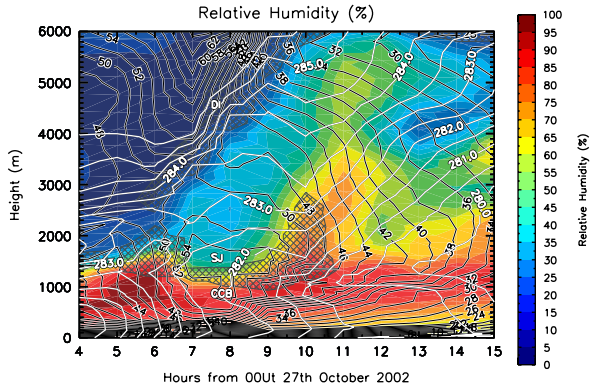

Figure 25. A synthesis of data from the enhanced UM above the pseudo-Cardington site (see text for details). Relative humidity is shown by the coloured contours, while black lines depict isotachs at 2 m s^{-1} intervals. The white lines are θ_w (white) contours every 0.5 K and the hashed regions depict areas of dry potential vorticity $\geq$ 1.5 PV units. Regions identified as the cold conveyor belt, sting jet and dry intrusion are marked CCB, SJ and DI respectively. This figure is available in colour online at www.interscience.wiley.com/journal/qj

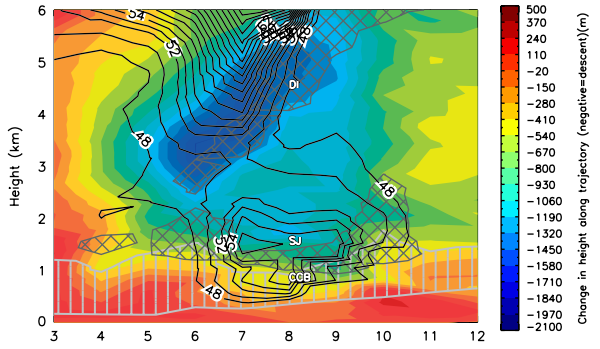

Figure 26. Time–height plot showing changes in height along trajectories initiated every hour above the pseudo-Cardington site from 0300 UTC to 1200 UTC. Each trajectory was taken back 5 hours over 4 minute time steps. Overlayed are isotachs (black contours at 48, 50 and every 1 m s^{-1} thereafter. Hashed regions depict areas of dry potential vorticity $\geq$ 1.5 PV units, and the vertically striped region depicts RH $>$ 80%. CCB, SJ and DI are as Figure 25). This figure is available in colour online at www.interscience.wiley.com/journal/qj

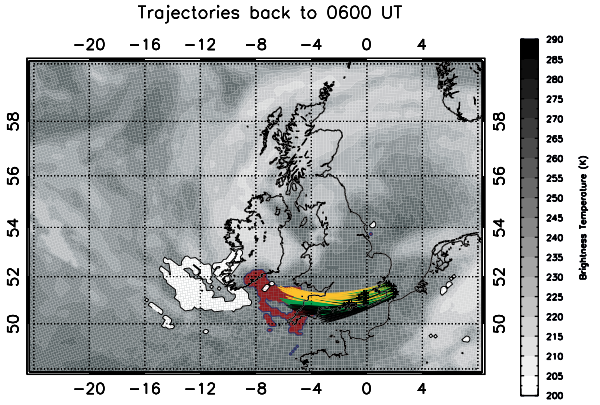

Figure 27. Trajectories back to 0600 UTC overlaid on to broadband infrared and single-jet feature-finding algorithm at 0600 UTC. See text for details. This figure is available in colour online at www.interscience.wiley.com/journal/qj

airflows – the descending (and therefore dry) sting jet and the moister CCB beneath it.

To check whether this interpretation is consistent with the history of air parcels within the model, the origins of the air above and below the PV anomaly were explored using back trajectories. These were initiated above the pseudo-location every 25 mb in height and at every hour, stepping back over 5 hours using 4 minute steps. Figure 26 shows that over the previous 5 hours the dry intrusion descended by up to 2100 m, and the dry low-level wind maximum experienced descent of around 1300 m. Figure 27 shows trajectories initiated at 850 (black), 750 (green) and 650 mb (orange) around the Cardington pseudo-location, taken back to 0600 h and compared with the areas returned by the two algorithms described in section 7.3. It is clear that all of these trajectories go back to the area identified as a sting jet over the Bristol Channel, Devon and Cornwall, confirming that the model fields depict the sting jet between 1 and 2 km over Cardington.

Below the dry wind maximum identified as the sting jet in Figure 25 there is a region of strong winds that has descended less than 500 m, i.e. this air remained near the top of the boundary layer, consistent with the cold conveyor belt. As in Figure 9 for the MST radar measurements, the model shows a region of elevated PV between the sting jet and CCB. Thus the model suggests that the wind maximum measured by the UFAM radar consisted of two distinct components, with the descending sting jet overlaying the recirculating CCB, and arriving at Cardington slightly earlier.

The radar measured very little wind shear in the bottom kilometre, with frequent convective plumes consistent with the unstable lowest layer in the radiosonde profile. To examine whether the model reproduced this wind structure, the wind shear at each grid point at 0800 h, calculated between model levels near 100 and 500 m, is shown in Figure 28. Over the whole of southern England strong low-level wind shear is present, in marked contrast to the observations. A clue to the origin of the discrepancy is afforded by the obvious association between wind shear and land surface in Figure 28 – the shear is almost zero over the Irish Sea, for instance, but jumps to 30 m s^{-1} km^{-1} over the Welsh coast. This points to a fault in the model parametrization of turbulence at the lowest levels.

9. Conditional symmetric instability

Conditional Symmetric Instability (CSI) was proposed by Browning (2004) and Clark *et al.* (2005) as a mechanism for sting jet generation. To locate all areas within the model where CSI might be present, and would be released (through upward motion), a diagnostic was constructed based on the algorithms of Dixon (1999). The aim of the diagnostic was to use the ingredients-based methodology in the review by Schultz and Schumacher (1999) to locate areas where CSI was present and being released. This identified areas where there was instability, moisture and lift, all necessary components for CSI, and distinguished areas susceptible to CSI from those also susceptible to gravitational and inertial instabilities. Thus each grid

DOI: 10.1002/qj

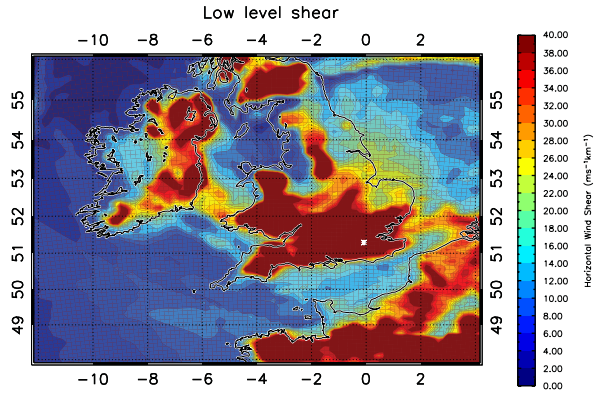

Figure 28. Low-level horizontal wind shear at 0800 UTC calculated using the wind fields at around 100 and 500 m. The location of the pseudo-UHF radar site is marked by a white star, clearly showing that it was located in a region of strong low-level wind shear. This figure is available in colour online at www.interscience.wiley.com/journal/qj

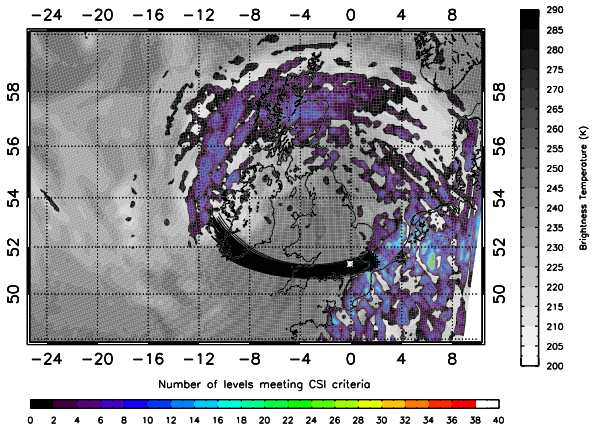

Figure 29. Trajectories initiated at 800 mb around the Cardington pseudo-location and taken back to 2300 h, overlaid on to simulated broad-band infrared and conditional symmetric instability diagnostic at 2300 h model time on 26 October. The white star denotes the Cardington pseudo-location. This figure is available in colour online at www.interscience.wiley.com/journal/qj

point within the model was examined for the following criteria.

(1) Geostrophic moist potential vorticity $MPV_g < 0$. This locates all areas of conditional, inertial and gravitational instability.
(2) $d\theta_e/dp < 0$. Removes areas of gravitational instabilities.
(3) Geostrophic relative vorticity + $f < 0$. Removes areas of inertial instabilities.
(4) Relative humidity $\geq 95\%$. Ensures that moisture is present.
(5) $w > 0$. Locates areas of lift.

Generally, areas of CSI were diagnosed parallel to the frontal regions as would be expected, following the curvature of the cloud head and terminating at its tip. CSI remained within the cloud head at all times of the model run, with its southernmost extent around 2300 h model time on 26 October. Back trajectories from the sting jet over the Cardington pseudo-location emanate from this region (Figure 29). This proximity between the tip of the CSI and the back trajectories persisted for the next two hours before the trajectories advanced ahead of the cloud-head tip. This is coincident with the transition to descent and the onset of drying and acceleration along the trajectories. As discussed earlier, there was no decrease of potential temperature during this period, consistent with the theory of CSI circulations that the most unstable downward branch is expected to remain isentropic. (Such descent is also expected to occur over a larger area than the narrow updrafts and, therefore, have a rate of descent smaller than the moist updrafts.)

Evidence of the narrow, moist updrafts is seen by the narrow width of the bands in the CSI diagnostic in Figure 29. This is consistent with the argument that the banding within the cloud head seen in satellite imagery was also CSI-generated. CSI is also consistent with the vertical banding along θ_w surfaces inferred from the MST radar. These bands were not coincident with the cores of the strongest winds, but were located between the wind cores, and so could be an indication of the upward-moving branches of the CSI circulations.

The evidence presented here is necessarily circumstantial and does not prove that CSI caused the sting jet; further investigation is required to identify a causal link. Nevertheless, given the proximity of the sting jet trajectories to the tip of the areas of active CSI, that these trajectories follow θ surfaces and that banding was seen in both the satellite and MST radar data, we cannot rule out a role for CSI in the generation of the sting jet.

10. Summary and conclusions

We have presented observations from two radar wind profilers of strong winds experienced in the mid and lower troposphere after the cold frontal passage of Windstorm Jeanette. This was a storm that evolved according to the Shapiro–Keyser paradigm, with frontal fracture and a prominent bent-back warm front. The depression centre passed just north of the UK MST radar at Aberystwyth in West Wales. As the tip of the bent-back cloud head passed over the site, the radar measured two wind maxima between 2 and 5 km, with prominent slantwise banding in both winds and echo power. Maximum wind speeds in these bands were up to 50 m s^{-1}, and the structure persisted into the clear air west of the cloud head. Both weather radar and satellite images showed horizontal banding in and around the cloud head as it passed Aberystwyth. Farther east, a UHF profiler based at Cardington in eastern England measured winds in excess of 40 m s^{-1} above 1 km for about 7 hours, as the cloud head passed this site. Very little wind shear was measured in the lowest kilometre, and the radar observed short-lived (< 10 min) plumes of high wind speed descending towards the surface, consistent with the increased gustiness observed at the ground. A radiosonde ascent at Nottingham, 120 km away but in the same airflow, showed a near-neutral boundary layer

DOI: 10.1002/qj

below 1 km with saturated air above, and satellite images showed low-level convection behind the cloud head.

To examine the origin of these features, the radar data were compared with two simulations by the UK Met Office UM. The operational configuration produced a reasonable simulation of the passage of the storm over Aberystwyth, and suggested that the banding in observed echo power lay along θ_w surfaces. However, closer inspection of the wind maxima in the model fields suggested that their occurrence resulted from the assimilation of radar data into the model analysis, and that the model dynamics alone were not able to reproduce the observed features. Following a similar conclusion drawn by Clark *et al.* (2005), a special run of the model with enhanced vertical resolution (90 vertical levels rather than 38) and a wider domain was used to simulate the event. Although this simulation of the storm evolved more rapidly than in reality, it was able to generate similar mid-level wind features to those seen by the radar: specifically, a single wind maximum (sting jet) in the midtroposphere followed by a double maximum extending westward away from the cloud head.

Algorithms were developed to map the extent of these features, and trajectory calculations used to explore their origin and development. Trajectories corresponding to the sting jet were found to descend ahead of the cloud-head tip, gaining momentum as they did so, and passing over the Cardington pseudo-site. Trajectories at the base of the sting jet remained isentropic, but a number of those in the upper half moistened with a lowering of θ, consistent with evaporation of precipitation falling into the air rather than mixing with moister (and potentially warmer) air above.

The model suggests that the strong winds measured at Cardington resulted from a merging of the descending sting jet with the cold conveyor belt travelling around the southern quadrant of the storm. This prolonged and possibly intensified the damaging winds experienced in Eastern England, emphasizing the importance of being able to forecast in detail the structure of storms of this type. The air identified with the sting jet, with low RH because of its descent, was separated from the moist CCB beneath it by a moist region of elevated potential vorticity. Such a region was also present in the model at Aberystwyth, separating the observed wind features from the CCB, which was too low down for the radar to observe. As the elevated PV coincided mainly with moist air, its origin would have been diabatic processes in the troposphere rather than stratospheric intrusion. Further investigations of other cases are needed to determine whether this is a regular feature of sting jets or a particular feature of this case.

The model predicted far stronger wind shear in the bottom 500 m than observed, and it seems that vigorous convection (as observed by the radar and satellites) kept this surface layer well mixed. Indeed, radar measurements of vertical winds (Figure 13) show convective plumes extending at least to 2 km, suggesting active mixing throughout this region and providing a mechanism for bringing the sting jet winds to the surface. It is clear that the ability of the UM to forecast damaging surface winds in such storms as these requires improvements in the simulation of low-level convection and mixing.

We draw the following conclusions from this study.

(1) The MST radar measured (for the first time) winds up to 50 m s^{-1} in the midtroposphere at the tip of the cloud head associated with the bent-back warm front of a storm developing according the the Shapiro–Keyser model of cyclogenesis.
(2) These observations are consistent with the notion of a sting jet developing in this region.
(3) The formation of a sting jet is not limited to the initial deepening phase of a storm.
(4) The sting jet region displayed a pronounced vertical and horizontal banding, with wind structures parallel to θ_w surfaces.
(5) This banding could be reproduced by the Met Office UM with enhanced vertical resolution.
(6) The horizontal and vertical scales of the observed structures are compatible with the notion of slantwise convection releasing CSI within the cloud head.
(7) The UFAM wind profiler at Cardington measured an extended wind maximum below 2 km, caused by a merger of the sting jet and the recirculating cold conveyor belt.
(8) The lowest kilometre of the atmosphere at Cardington was well-mixed, with pronounced convective plumes. These plumes extended into the sting jet region and were responsible for damaging gusts at the surface.
(9) The depiction of the surface layer by the UM predicted far more low-level wind shear than observed, pointing to improvements necessary in the simulation of downward momentum transport in such events as these.

Acknowledgements

We thank the NERC MST radar facility for the radar data used here, and Davey Hooper for processing the data to mitigate interference effects. Chang-Gui Wang helped with model data extraction, and other satellite and meteorological data were provided by the British Atmospheric Data Centre and the NERC Satellite Data Centre, Dundee. GP was supported by a NERC PhD studentship. We also thank two anonymous referees for their comments on the original manuscript.

References

Browning KA. 1990. Organization of clouds and precipitation in extratropical cyclones. *Extratropical Cyclones: The Eric Palmén Memorial Volume*, Newton C, Holopainen E (eds). American Meteorological Society: Boston. pp 81–105.

Browning KA. 2004. The Sting at the end of the tail: Damaging winds associated with extratropical cyclones. *Q. J. R. Meteorol. Soc.* **130**: 375–399.

Browning KA. 2005. Observational synthesis of mesoscale structures within an explosively deepening cyclone. *Q. J. R. Meteorol. Soc.* **131**: 603–623.

Browning KA, Field M. 2004. Evidence from Meteosat imagery of the interaction of sting jets with the boundary layer. *Meteorol. Appl.* **11**: 277–289.
Clark PA, Browning KA, Wang C. 2005. The Sting at the end of the tail: Model diagnostics of fine-scale 3D structure of the cloud head. *Q. J. R. Meteorol. Soc.* **131**: 2263–2292.
Dixon R. 1999. *Diagnostic studies of symmetric instability.* PhD thesis, Univ. Reading.
Ducrocq V. 1993. Adiabatic and viscous simulations of symmetrical instability – structure, evolution, and energetics. *J. Atmos. Sci.* **50**: 23–42.
Gage KS, Balsley BB, Green JL. 1981. Fresnel scattering model for the specular echoes observed by VHF radar. *Radio Sci.* **16**: 1447–1453.
Grønås S. 1995. The seclusion intensification of the New Years Day storm 1992. *Tellus* **47A**: 733–746.
Norton EG, Vaughan G, Methven J, Coe H, Brooks B, Gallagher M, Longley I. 2006. Boundary layer structure and decoupling from synoptic scale flow during NAMBLEX. *Atmos. Chem. Phys.z* **6**: 433–445.
Ottersten H. 1969. Mean vertical gradient of potential refractive index in turbulent mixing and radar detection of CAT. *Radio Sci.* **4**: 1247–1249.
Persson POG, Warner TT. 1993. Nonlinear hydrostatic conditional symmetric instability – implications for numerical weather prediction. *Mon. Weather Rev.* **121**: 1821–1833.
Reid HL, Vaughan G. 2004. Convective mixing in a tropopause fold. *Q. J. R. Meteorol. Soc.* **130**: 1195–1212.
Sanders F, Guyakum J. 1980. Synoptic-dynamic climatology of the 'bomb'. *Mon. Weather Rev.* **108**: 1589–1606.
Schultz D, Schumacher P. 1999. The use and misuse of conditional symmetric instability. *Mon. Weather Rev.* **127**: 2709–2732.
Shapiro MA, Keyser D. 1990. Fronts,jet streams and the tropopause. *Extratropical Cyclones: The Erik Palmén Memorial Volume*, Newton C, Holopainen E (eds). American Meteorological Society: Boston. pp 167–191.
Vaughan G. 2002. The UK MST Radar. *Weather* **57**: 69–73.

DOI: 10.1002/qj